Effects of dispersion in tsunami Green's functions and implications for joint inversion with seismic and geodetic data: a case study of the 2010 Mentawai M_W 7.8 earthquake

Linyan Li[1], Kwok Fai Cheung[1,*], Han Yue[2], Thorne Lay[3], and Yefei Bai[1]

[1]Department of Ocean and Resources Engineering, University of Hawaii at Manoa, Honolulu, HI, USA.

[2]Seismological Laboratory, California Institute of Technology, Pasadena, CA 91125, USA.

[3]Department of Earth and Planetary Sciences, University of California Santa Cruz, Santa Cruz, CA 95064, USA.

*Corresponding author: Kwok Fai Cheung (cheung@hawaii.edu)

Key Points:

- Modeling of tsunami generation from seafloor deformation leads to depth-dependent attenuation and spreading of the initial waves at the source
- Dispersion complements depth-dependent tsunami excitation through lagging of short-period components during trans-oceanic propagation
- Including depth-dependent tsunami excitation and dispersion in Green's functions results in larger and more concentrated slip through inversion

Abstract

Tsunami observations play an important role in resolving offshore earthquake slip distributions. Non-dispersive models are often used with an initial static sea-surface pulse derived from seafloor deformation in computation of tsunami Green's functions. We compare this conventional approach with more advanced techniques, which use Green's functions computed by a dispersive model with an initial static sea-surface pulse and with the surface waves generated from kinematic seafloor deformation. These three sets of tsunami Green's functions are implemented in finite-fault inversions with and without seismic and geodetic

This article has been accepted for publication and undergone full peer review but has not been through the copyediting, typesetting, pagination and proofreading process which may lead to differences between this version and the Version of Record. Please cite this article as doi: 10.1002/2016GL070970

data for the 2010 Mentawai M_W 7.8 tsunami earthquake. Seafloor excitation and wave dispersion produce more spread-out waveforms in the Green's functions leading to larger slip with more compact distribution through the inversions. The fit to the recorded tsunami and the deduced seismic moment, which reflects the displaced water volume, are relatively insensitive to the approach used for computing Green's functions.

1. Introduction

Tsunami recordings are commonly used alone or with geodetic and seismic data to resolve earthquake rupture through finite-fault inversion. Non-dispersive shallow-water modeling has been an established approach in computation of tsunami Green's functions for earthquake source investigation and far-field wave forecasting [*Satake*,1987,1989; *Satake et al.*, 2013; *Wei et al*., 2003, 2014]. This hydrostatic approach utilizes a static initial sea-surface pulse derived from seafloor deformation and describes wave propagation through the shallow-water celerity independent of the period. Modeling of tsunami generation from kinematic seafloor deformation has indicated attenuation of the initial sea-surface elevation depending on the water depth at the source [*Grilli et al*., 2013; *Lay et al*., 2013a, 2013b; *Saito*, 2013; *Yamazaki et al*., 2011]. In addition, observations have shown effects of dispersion characterized by lagging of short-period components and reduction of the leading wave amplitude during trans-oceanic propagation [*Hanson and Bowman*, 2005; *Saito et al*., 2010].

The role of tsunami dispersion in source model inversion has received attention in recent years. *Saito et al.* [2010] and *Hossen et al.* [2015] demonstrated effects of dispersion on predicted tsunami source areas using Green's functions generated by static initial pulses as finite sources on the sea surface, while *Saito et al.* [2011] estimated the initial sea-surface elevation for the 2011 Tohoku tsunami through inversion of the near-field DART and GPS records. Their Green's functions were generated by Boussinesq models, which describe dispersion through high-order terms derived from the horizontal flow velocity. *Romano et al.* [2012, 2014] performed joint inversion of a finite-fault model using tsunami and geodetic records of the 2011 Tohoku event and accounting for dispersion through the non-hydrostatic

NEOWAVE model of *Yamazaki et al.* [2009, 2011]. For propagation across open oceans, a frequency-dependent phase correction can incorporate dispersion effects into Green's functions computed by hydrostatic models [*Gusman et al.*, 2014; *Yoshimoto et al*., 2015; *Yue et al*., 2014a].

Depth-dependent tsunami excitations across the water column also influence the Green's functions. *Bletery et al.* [2014] implemented a reduction factor from *Kajiura* [1963] to define the static initial sea-surface elevation from seafloor deformation and utilized NEOWAVE to generate Green's functions for joint inversion of a finite fault model with geodetic, seismic, and tsunami records from the 2011 Tohoku event. NEOWAVE describes dispersion through the vertical velocity, which facilitates modeling of kinematic seafloor deformation to provide a more complete account of tsunami generation. The use of the vertical velocity instead of high-order horizontal velocity terms results in a simple numerical framework that allows implementation of two-way nested grids for modeling of physical processes across a wide range of scales [*Yamazaki et al*., 2012; *Cheung et al*., 2013; *Bai and Cheung*, 2016a]. *Yue et al.* [2015] utilized these capabilities to compute Green's functions for joint inversion of the 2010 Mentawai M_W 7.8 earthquake. The resulting finite-fault model shows large, concentrated slip near the trench that is not evident in other studies.

There are three general approaches to compute tsunami Green's functions: hydrostatic and non-hydrostatic modeling with a static initial sea-surface pulse derived from seafloor deformation as well as the more accurate non-hydrostatic modeling with kinematic seafloor excitation from the earthquake rupture. While there is no doubt that dispersion occurs during tsunami generation and propagation, the importance of accounting for these effects in source model inversions has not been clearly demonstrated. We investigate this problem using finite-fault inversions of tsunami, geodetic, and seismic data from the 2010 Mentawai event. NEOWAVE can perform hydrostatic and non-hydrostatic computations with static or kinematic descriptions of the tsunami source. The use of the same code and nested grid system allows systematic examination of the three types of Green's functions and their influences on the inversion results.

2. Methodology and Data

The 25 October 2010 M_W 7.8 thrust earthquake ruptured the shallow portion of the Sunda megathrust. Figure 1a shows the location of the epicenter (3.49°S, 100.14°E) seaward of the Mentawai Islands offshore of Sumatra. The earthquake generated a destructive tsunami with 3-9 m runup on Pagai and up to 16.9 m on the small island of Sibigau [*Hill et al.,* 2012]. The disproportionately large tsunami is attributed to concentrated slip on the shallow megathrust near the trench, which is characteristic of a tsunami earthquake [*Yue et al.,* 2014b]. *Yue et al.* [2015] provided a detailed description of the recorded geophysical and hydrographic datasets used here for finite-fault inversion of the source. These include 53 *P*-wave and 24 *SH*-wave ground displacements from stations of the Federation of Digital Seismic Networks (FDSNs), three-component ground motions from 12 high-rate SuGAr GPS stations on the Mentawai Islands, and tsunami waveforms at two deep-water stations (GITEWS GPS 03 and DART 56001) and two tide gauges (Cocos Island and Padang).

Yue et al. [2015] described in detail the finite-fault model and parameterization for the joint inversions. As illustrated in Figure 1b, the subfaults are arranged in 7 rows along dip and 15 columns along strike with dimensions of 15 km by 15 km each. The fine model grid is selected to resolve the concentrated near-trench slip of the tsunami earthquake. The fault has a uniform dip angle of 7.5º based on the shallow megathrust reflection profile of *Singh et al.* [2011]. The source time function of each subfault is parameterized by five triangles with durations of 4 s shifted by 2 s sequentially for a total possible duration of 12 s. The teleseismic Green's functions are generated with a reflectivity method that accounts for interaction in 1-D layered structures on both the source and receiver sides [*Kikuchi et al.,* 1993]. A local 1-D layered model based on the reflection imaging is used for the source side and a typical continental model is used for the receiver side. The near-field time-varying ground displacement Green's functions are computed using a frequency-wave number integration method [*Hermann,* 2013]. The same band-pass filter is used for the Green functions and records of each type.

We utilize NEOWAVE to compute tsunami Green's functions at the four water-level stations for unit slip vectors with 45° and 135° rake. The two-way nested computational grids have resolution varying from 1 arc-min (~1800 m) across the Eastern Indian Ocean to 12 arc-s (~360 m) in the source region around the Mentawai Islands, 1.5 arc-s (~45 m) at Cocos Island, and 0.3 arc-s (~9 m) at Padang Harbor, as illustrated in Figure 1. The half-space model of *Okada* [1992] provides the seafloor deformation for 1-m slip of each subfault and the method of *Tanioka and Satake* [1996] augments the vertical seafloor motion to account for horizontal displacement on bathymetric slopes. The total vertical displacement defines the static initial sea-surface elevation for computation of the first two sets of Green's functions using the hydrostatic and non-hydrostatic implementations of NEOWAVE. For the third set, we approximate the time history of the kinematic seafloor vertical displacement by a linear function over a 4-s duration to provide a boundary condition for non-hydrostatic modeling of tsunami generation and propagation. Although NEOWAVE includes nonlinear effects, the sea-surface waves generated by 1-m slip have very small amplitude comparing to the wavelength and water depth. *Yue et al.* [2015] showed the resulting Green's functions are not sensitive to the assumed rise time and can be combined linearly with time-shift increments of 4 s to reconstruct recorded tsunamis generated by a rupture sequence.

3. Tsunami Green's Functions

The 105 subfaults, two slip vectors, four stations, and the three modeling approaches result in 2520 tsunami Green's functions. Figure 2 plots the maximum surface elevations for unit slip with 45° rake of subfaults 15, 45, and 90, which extend across the continental slope (Figure 1b). The small subfault size presents a challenge to both hydrostatic and non-hydrostatic modeling. The contrast between the three approaches is most pronounced for subfault 15 beneath the trench. The deep water of 5000 m and shallow fault depth of 2.2 km into the rock result in a large ratio of water depth to wavelength, the latter of which is associated with the dimensions of the seafloor deformation. The absence of direct seafloor excitation and wave dispersion in the hydrostatic approach (H-S) leads to higher estimation of the surface elevation from the source to the far field. The non-hydrostatic approach with the static initial

pulse (Nh-S) has the same surface elevation at the source, but produces more rapid amplitude decrease to the far field due to dispersion. Inclusion of kinematic seafloor deformation (Nh-K) accounts for depth-dependent excitation across the water column, resulting in smaller wave amplitude at both the source and in the far field. The tsunami excitation and dispersive wave processes play a lesser role for the deeper subfault 45, which has more spread-out seafloor deformation in shallower water. The three approaches produce very similar results for subfault 90 further down dip, where the water depth is only 500 m and the fault depth is 12.7 km. The small water-depth to wavelength ratio provides an explanation for the minor effects of dispersion in the resulting surface elevation.

Dispersion influences the waveforms in addition to the amplitude. Figure 3 compares the three sets of Green's functions from subfaults 10, 13, 15, 45 and 90 at the four water-level stations. In Figure 3a, the Green's functions at the GPS buoy illustrate effects of dispersion in the near field. The buoy is located directly above subfault 15 at the trench, where the seafloor excitation produces a much smaller peak than the initial surface pulse determined from seafloor deformation. Both non-hydrostatic approaches produce oscillations at the source albeit with different phases. The shorter and steeper pulse from the static initial condition is more dispersive. Free fall of the larger, initial sea-surface wave produces more energetic oscillations, but the amplitude attenuates more rapidly in time and space. The phase of the radiated waves approaches that generated by seafloor excitation away from the source as can be inferred from the Green's functions of subfaults 13 and 10 along the trench. The short-period trailing oscillations in the range of dispersive waves are caused by the pointed seafloor uplift from the half-space solution for the shallow subfaults. The Green's functions for subfaults 45 and 90, which are located landward beneath the continental slope, show decreasing dispersion effects due to the shallower water and longer pulse associated with the increasing fault depth. In comparison, the hydrostatic solution shows negligible surface oscillations after the initial upswing even for subfaults 10, 13, and 15 located along the trench.

The Green's functions in the far field reflect mostly the propagation processes. Numerical dispersion is small in the non-hydrostatic solution for the wave period range and grid

resolution involved [*Bai and Cheung*, 2016b]. At the Padang tide gauge as shown in Figure 3b, the two non-hydrostatic approaches produce the same phase from all five subfaults albeit with slightly smaller amplitude obtained with the kinematic seafloor excitation. The hydrostatic approach produces a similar Green's function for subfault 90, but shows increasing discrepancies relative to the non-hydrostatic predictions for subfaults further up-dip. The two sets of non-hydrostatic Green's functions show improved agreement of the amplitude away from the source as indicated in the comparisons at Cocos Island and DART 56001 in Figures 3c and 3d. With the exception of subfault 90, the hydrostatic Green's functions show prominent high-frequency numerical oscillations sensitive to the computational grid resolution (Figure S1 in the Supporting Information). The shallower fault depth and deeper water down the continental slope together with the fine rupture model result in short-period tsunami signals not adequately resolved by the hydrostatic model. When the Green's functions from the subfaults are combined, the tsunami signal increases in both amplitude and period with diminishing dispersion effects and numerical oscillations for the larger rupture area (Figures S2 and S3). Filtering removes the numerical oscillations below 3 min period to isolate the tsunami signals observed in the non-hydrostatic solutions (Figure S4). The resulting time series indicates simultaneous arrival of long and short-period waves, while the two non-hydrostatic solutions show lagging of the short-period waves due to lower propagation speeds associated with dispersion.

4. Results and Discussion

We utilize the same datasets of the 2010 Mentawai M_W 7.8 earthquake from *Yue et al.* [2015] to examine the sensitivity of finite fault inversion to the three types of tsunami Green's functions. The *P* and *SH* waves are sampled at 0.5 s intervals over a 120-s window starting 10 s prior to arrivals. Each trace of the Hr-GPS records has a 200-s window sampled at 1-s intervals starting at the origin time of the hypocenter. The recorded tsunami arrivals at the Padang and Cocos Island tide gauges are 2 and 4 min ahead of the model results and are shifted accordingly to offset the timing discrepancy, which we attribute to bathymetric inaccuracies. The recorded waveforms, which have varying amplitudes among the four

stations, are adjusted by scaling parameters to achieve consistent weights in the inversion. When the filtered hydrostatic Green's functions at Cocos Island and DART 56001 are used in the inversion, the corresponding records are filtered in the same way to avoid projection of any artifacts into the solution. A rupture velocity of 2.0 km/s expanding from the hypocenter defines the rupture initial time at each subfault. The finite-fault inversion involves solving for space-time varying weights of the Green's functions to match the recorded datasets through a non-negative linear least squares approach.

Figure 4 compares the observed and predicted waveforms at the four water-level stations from the tsunami-only and joint inversions. The inversion time windows include the initial double peaks at the GPS buoy, the first two waves at Padang and Cocos Island, and the dominant long-period pulse at the DART buoy. The waveforms in these time intervals provide information most relevant to the source. The overall fits within the time windows are quite good. All three types of Green's functions produce similar results despite their varying waveforms at the stations. As long as the model representation has sufficient degrees of freedom, the least squares approach can produce a good fit to the observations with the variations among the Green's functions compensated by the source model. The numerical oscillations in the hydrostatic Green's functions do not appear to interfere with the fitting of the tsunami signals, but do show up subsequently in the predicted waveforms. The discrepancy between the recorded and predicted waveforms also increases outside the inversion time windows. The two sets of non-hydrostatic Green's functions maintain very similar predictions, while the filtered hydrostatic Green's functions produce comparable amplitude with a notable phase shift. The joint inversion results show slightly larger deviations from the records due to the intrinsic need to reconcile multiple datasets that might not be fully compatible.

The inversions provide the slip distributions shown in Figure 5. All slip models involve primary rupture propagation up dip and along strike in the northwest direction. The detailed slip distribution varies significantly with the type of Green's functions used in the inversion despite the similar fits to the tsunami observations. For the tsunami-only inversion in Figure

5a, the non-hydrostatic Green's functions resolve the large concentrated slip extending along the trench. The model with kinematic seafloor excitation has maximum slip of 15.9 m, while the static initial condition results in a lower value of 13.6 m as needed to account for the absence of wave attenuation at the source. Filtering is necessary for the hydrostatic Green's functions that have increasing numerical oscillations for subfaults near the trench. The alignment of the frequency components due to the lack of dispersion is compensated by a more spread-out slip distribution and a further reduction of the maximum slip to 10.0 m. Without filtering, the inversion suppresses the numerical oscillations to fit the recorded waveforms by spreading the slip more evenly down dip. This results in relatively small slip of less than 5.8 m near the trench. The cumulative seismic moments for the four predictions are still close, in the range of 8.9 to 9.2×10^{20} Nm (M_W 7.90-7.91).

The results from the joint inversion in Figure 5b show similar effects of the tsunami Green's functions, but with more focused slip distributions along the trench (see Figures S5 and S6 for sample comparisons of geodetic and seismic datasets). The inversions with non-hydrostatic Green's functions produce maximum slip of 15.7 and 13.3 m comparable to the tsunami-only inversions. In the absence of dispersion in the tsunami Green's functions, the seismic and geodetic datasets play a more significant role in defining the slip along the trench. The joint inversion gives maximum slip of 8.4 m when the filtered Green functions are used. When the near-trench slip is suppressed and spread down dip through the use of the unfiltered hydrostatic Green's functions, the geodetic and seismic datasets help maintain the maximum slip at 7.1 m. The cumulative moments of $7.5\text{-}8.3\times10^{20}$ Nm (M_W 7.85-7.88) are consistently lower than those of the tsunami-only inversions indicating reconciliation among the tsunami, geodetic, and seismic datasets through the inversion process.

5. Conclusions

The slip distributions of the 2010 Mentawai earthquake inverted using the three types of tsunami Green's functions differ significantly even though they have comparable total seismic moments and similar fits to the tsunami recordings. This makes it difficult to assess

the validity of source models from the predicted waveforms and emphasizes the need to properly account for tsunami generation and propagation processes. The Green's functions computed using a non-hydrostatic model with either kinematic seafloor excitation or static initial conditions improve resolution of concentrated near-trench slip. Depth-dependent tsunami excitation influences the amplitude and phase of the Green's functions close to the source, providing better resolution of the slip when near-field observations are available.

Assumption of the initial sea surface elevation based on coseismic seafloor deformation is implicit in the Green's functions generated by the hydrostatic approach. The shallow fault depth near the trench results in short-period waves generated in relatively deep water. The hydrostatic model overestimates the initial wave amplitude from seafloor displacement, forces the frequency components to remain aligned during propagation, and introduces high-frequency numerical oscillations at far-field station. In matching the tsunami recordings, the inversion acquires an excessively smoothed slip distribution to suppress the numerical oscillations in the synthetics. Even with filtering, the hydrostatic Green's functions still produce spread-out, lower amplitude slip to compensate for the lack of dispersion. Non-hydrostatic tsunami calculations are clearly warranted for reliable imaging of detailed slip distributions.

Acknowledgments. The IRIS data management center was used to access the seismic data from Global Seismic Network and Federation of Digital Seismic Network stations. The hr-GPS data was recorded by the SuGAr network jointly operated by the Earth Observatory of Singapore and the Indonesia Institute of Sciences. The GITEWS GPS buoy data in Mentawai were provided by the Badan Meteorology and Geofisika (BMKG), Indonesia. DART buoy data were obtained from the NOAA National Data Buoy Center. The digital elevation model is derived from the 30 arc-s General Bathymetric Chart of the Oceans compiled by the British Oceanographic Center; the 2 arc-s Digital Bathymetric Model of Badan Nasional Penanggulangan Bencana, Indonesia; 1 arc-s Shuttle Radar Topography Mission from German Aerospace Center; 0.15 arc-s LiDAR data at Padang from Badan Informasi Geospasial; and a 9 arc-s gridded data set in the Cocos Island region from Geoscience

Australia. L. Li, Y. Bai, and K.F. Cheung received support from National Tsunami Mitigation Program grant NA15NWS4670025, T. Lay was supported by NSF grant EAR1245717, and H. Yue was supported by a Caltech Seismological Director's fellowship. We thank the two anonymous reviewers for the comments and suggestions that have improved this paper. SOEST Contribution 9834.

References

Bai, Y. and K.F. Cheung (2016a), Hydrostatic versus non-hydrostatic modeling of tsunamis with implications for insular shelf and reef environments, *Coastal Eng.*, 117, 32-43.

Bai, Y. and K.F Cheung (2016b), Linear and nonlinear properties of reduced two-layer models for non-hydrostatic free-surface flow, *Ocean Modell.*, doi:10.1016/j.ocemode.2016.10.003, in press.

Bletery, Q., A. Sladen, B. Delouis, M. Vallée, J.-M. Nocquet, L. Rolland, and J. Jiang (2014), A detailed source model for the M_W 9.0 Tohoku-Oki earthquake reconciling geodesy, seismology and tsunami records, *J. Geophys. Res. Solid Earth, 119*, 7636–7653, doi:10.1002/2014JB011261.

Cheung, K.F., Y. Bai, and Y. Yamazaki (2013), Surges around the Hawaiian Islands from the 2011 Tohoku tsunami, *J. Geophys. Res. Oceans*, 118, 5703-5719, doi: 10.1002/jgrc.20413.

Grilli, S., J. Harris, T. Tajallibakhsh, T. Masterlark, C. Kyriakopoulos, J. Kirby, and F. Shi (2013), Numerical Simulation of the 2011 Tohoku tsunami based on a new transient FEM co-seismic source: Comparison to far- and near-field observations, *Pure Appl. Geophys.*, *170* (6–8), 1333–1359.

Gusman, A. R., Murotani, S., Satake, K., Heidarzadeh, M., Gunawan, E., Watada, S. and Schurr, B. (2015), Fault slip distribution of the 2014 Iquique, Chile, earthquake estimated from ocean-wide tsunami waveforms and GPS data. *Geophys. Res. Lett.*, 42, 1053–1060. doi: 10.1002/2014GL062604.

Hanson, J.A., and J.R. Bowman (2005), Dispersive and reflected tsunami signals from the 2004 Indian Ocean tsunami observed on hydrophones and seismic stations, *Geophys. Res. Lett., 32*, L17606, doi: 10.1029/2005GL023783.

Herrmann, R.B. (2013), Computer programs in seismology: An evolving tool for instruction and research, *Seism. Res. Lett.*, 84, 1081-1088, doi:10.1785/0220110096

Hossen, M. J., P. R. Cummins, J. Dettmer, and T. Baba (2015), Tsunami waveform inversion for sea surface displacement following the 2011 Tohoku earthquake: Importance of dispersion and source kinematics, *J. Geophys. Res. Solid Earth, 120*, 6452–6473, doi:10.1002/2015JB011942.

Hill, E. M., et al. (2012), The 2010 M_W 7.8 Mentawai earthquake: Very shallow source of a rare tsunami earthquake determined from tsunami field survey and near-field GPS data, *J. Geophys. Res., 117*, B06402, doi:10.1029/2012JB009159.

Kajiura, K. (1963), The leading wave of a tsunami, *Bull. Earthquake Res. Inst., 41*, 535–571.

Kikuchi, M., H. Kanamori, and K. Satake (1993), Source complexity of the 1988 Armenian earthquake: Evidence for a slow after-slip event, *J. Geophys. Res., 98*(B9), 15,797–15,808, doi:10.1029/93JB01568.

Lay, T., L. Ye, H. Kanamori, Y. Yamazaki, K. F. Cheung, K. Kwong, and K. D. Koper (2013a), The October 28, 2012 M_W 7.8 Haida Gwaii underthrusting earthquake and tsunami: Slip partitioning along the Queen Charlotte Fault transpressional plate boundary, *Earth Planet. Sci. Lett., 375*, 57–70, doi:10.1016/j.epsl.2013.05.005.

Lay, T., L. Ye, H. Kanamori, Y. Yamazaki, K. F. Cheung, and C. J. Ammon (2013b), The February 6, 2013 M_W 8.0 Santa Cruz Islands earthquake and tsunami, *Tectonophys., 608*, 1109–1121, doi:10.1016/j.tecto.2013.07.001.

Okada, Y. (1992), Internal deformation due to shear and tensile faults in a half-space, *Bull. Seismol. Soc. Am., 82*, 1018–1040.

Romano, F., A. Piatanesi, S. Lorito, N. D'Agostino, K. Hirata, S. Atzori, Y. Yamazaki, and M. Cocco (2012), Clues from joint inversion of tsunami and geodetic data of the 2011 Tohoku-oki earthquake, *Sci. Rep., 2*, 385, doi:10.1038/srep00385.

Romano, F., E. Trasatti, S. Lorito, C. Piromallo, A. Piatanesi, Y. Ito, D. Zhao, K. Hirata, P. Lanucara, and M. Cocco (2014), Structural control on the Tohoku earthquake rupture process investigated by 3D FEM, tsunami and geodetic data, *Sci. Rep., 4*, 5631, doi:10.1038/srep05631.

Saito, T. (2013), Dynamic tsunami generation due to sea-bottom deformation: Analytical representation based on linear potential theory, *Earth, Planets, and Space*, 65, 1411-1423.

Saito, T., K. Satake, and T. Furumura (2010), Tsunami waveform inversion including dispersive waves: the 2004 earthquake off Kii Peninsula, Japan, *J. Geophys. Res., 115*, B06303, doi:10.1029/2009JB006884.

Saito, T., Y. Ito, D. Inazu, and R. Hino (2011), Tsunami source of the 2011 Tohoku-Oki earthquake, Japan: Inversion analysis based on dispersive tsunami simulations, *Geophys. Res. Lett., 38*, L00G19, doi:10.1029/2011GL049089.

Satake, K. (1987), Inversion of tsunami waveforms for the estimation of a fault heterogeneity: Method and numerical experiments, *J. Phys. Earth, 35*, 241–254.

Satake, K. (1989), Inversion of tsunami waveforms for the estimation of heterogeneous fault motion of large submarine earthquakes: The 1968 Tokachi-Oki and the 1983 Japan Sea earthquakes, *J. Geophys. Res., 94*(B5), 5627–5636, doi:10.1029/JB094iB05p05627.

Satake, K., Y. Fujii, T. Harada, and Y. Namegaya (2013), Time and space distribution of coseismic slip of the 2011 Tohoku earthquake as inferred from tsunami waveform data, *Bull. Seismol. Soc. Am., 103*(2B), 1473–1492.

Singh, S. C., N. Hananto, M. Mukti, H. Permana, Y. Djajadihardja, and H. Harjono (2011), Seismic images of the megathrust rupture during the 25th October 2010 Pagai earthquake, SW Sumatra: Frontal rupture and large tsunami, *Geophys. Res. Lett., 38*, L16313, doi:10.1029/2011GL048935.

Tanioka, Y., and K. Satake (1996), Tsunami generation by horizontal displacement of ocean bottom, *Geophys. Res. Lett., 23*, 861–864, doi:10.1029/96GL00736.

Wei, Y., K.F. Cheung, G.D. Curtis, and C.S. McCreery (2003), Inverse algorithm for tsunami forecasts, *J. Waterw. Port, Coastal, Ocean Eng.*, 129(2), 60-69.

Wei, Y., A. V. Newman, G. P. Hayes, V. V. Titov, and L. Tang (2014), Tsunami forecast by joint inversion of real-time tsunami waveforms and seismic or GPS data: Application to the Tohoku 2011 tsunami, *Pure Appl. Geophys*., *171*(12), 3281-3305, doi:10.1007/s00024-014-0777-z.

Yamazaki, Y., Z. Kowalik, and K. F. Cheung (2009), Depth-integrated, non-hydrostatic model for wave breaking and run-up, *Int. J. Numer. Methods Fluids, 61*(5), 473–497.

Yamazaki, Y., K. F. Cheung, and Z. Kowalik (2011), Depth-integrated, non-hydrostatic model with grid nesting for tsunami generation, propagation, and run-up, *Int. J. Numer. Methods Fluids, 67*(12), 2081–2107.

Yamazaki, Y., K.F. Cheung, G. Pawlak, and T. Lay (2012), Surges along the Honolulu coast from the 2011 Tohoku tsunami. *Geophys. Res. Lett*, 39, L09604, Doi: 10.1029/2012GL051624.

Yoshimoto, M., S. Watada, Y. Fujii, and K. Satake (2016), Source estimate and tsunami forecast from far-field deep-ocean tsunami waveforms—The 27 February 2010 M_w 8.8 Maule earthquake, *Geophys. Res. Lett*., 43, 659–665, doi: 10.1002/2015GL067181.

Yue, H., T. Lay, L. Rivera, C. An, C. Vigny, X. Tong, and J. C. Báez Soto (2014a), Localized fault slip to the trench in the 2010 Maule, Chile M_w = 8.8 earthquake from joint inversion of high-rate GPS, teleseismic body waves, InSAR, campaign GPS, and tsunami observations, *J. Geophys. Res. Solid Earth*, 119, 7786–7804, doi:10.1002/2014JB011340.

Yue, H., T. Lay, L. Rivera, Y. Bai, Y. Yamazaki, K. F. Cheung, E. M. Hill, K. Sieh, W. Kongko, and A. Muhari (2014b), Rupture process of the 2010 M_W 7.8 Mentawai tsunami earthquake from joint inversion of near-field hr-GPS and teleseismic body wave recordings constrained by tsunami observations, *J. Geophys. Res. Solid Earth, 119*, 5574–5593, doi:10.1002/2014JB011082.

Yue, H., T. Lay, L. Li, Y. Yamazaki, K. F. Cheung, L. Rivera, E. M. Hill, K. Sieh, W. Kongko, and A. Muhari (2015), Validation of linearity assumptions for using tsunami waveforms in joint inversion of kinematic rupture models: Application to the 2010 Mentawai M_w 7.8 tsunami earthquake, *J. Geophys. Res. Solid Earth, 120*, 1728–1747, doi:10.1002/2014JB011721.

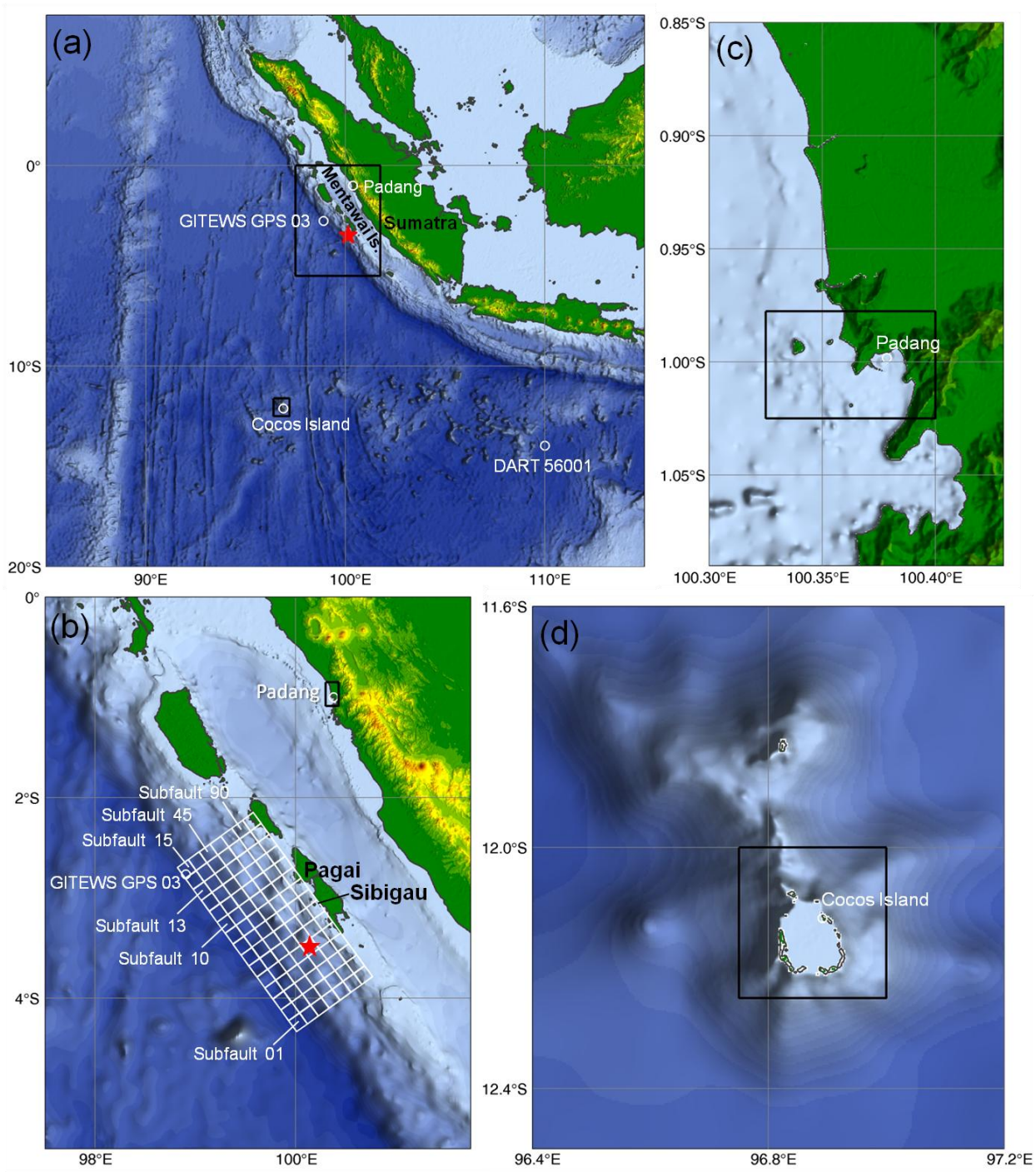

Figure 1. Location maps and computational grids. (a) Level-1 grid with outlines of level-2 grids around the rupture area and Cocos Island. Red star and white circles indicate the epicenter and water-level stations. (b) Level-2 grid with outlines of level-3 grid at Padang and the source model. (c) Level-3 grid with outline of level-4 grid at Padang Harbor. (d) Level-2 grid with outline of level-3 grid around Cocos Island.

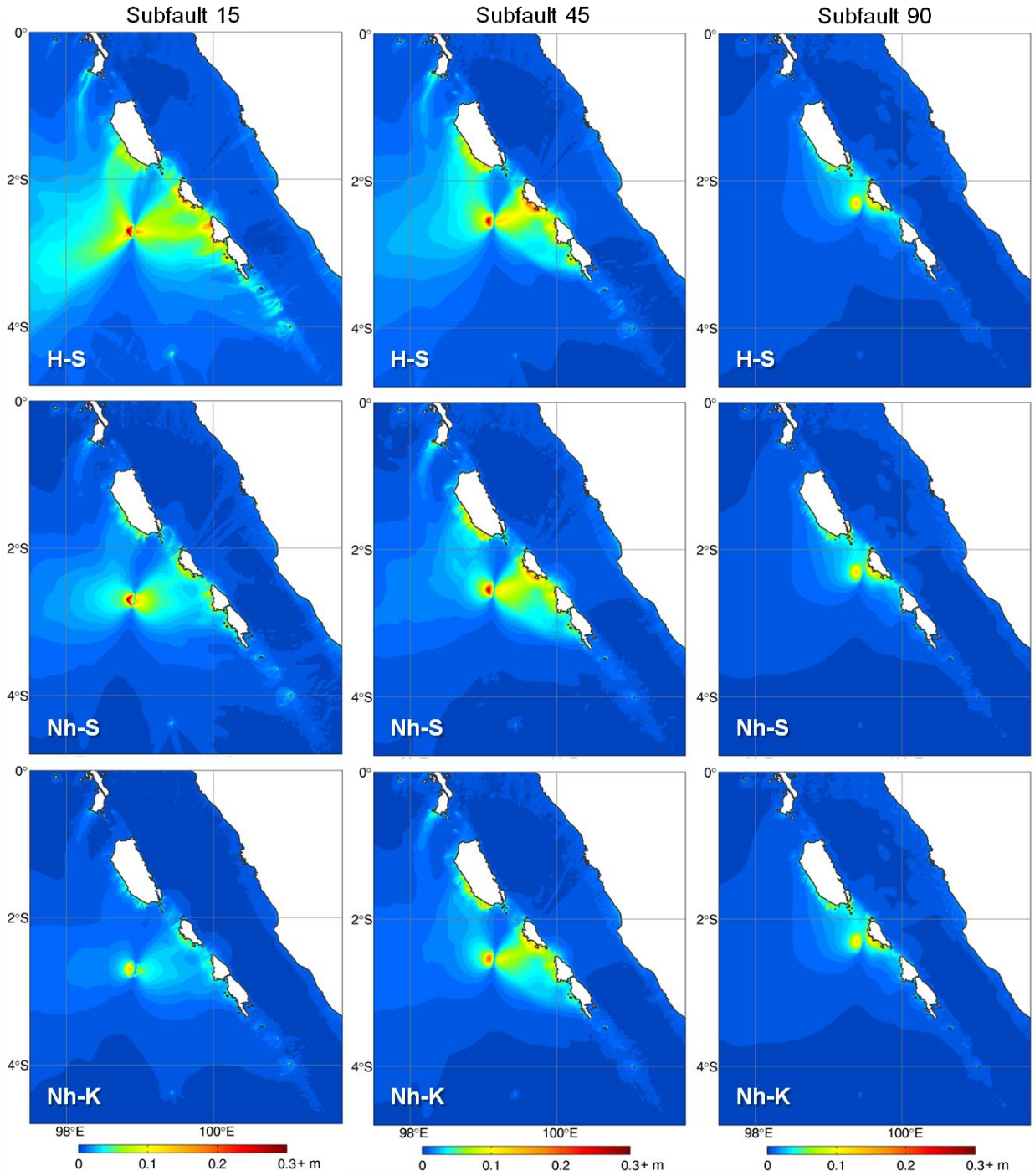

Figure 2. Maximum sea-surface elevations generated by the H-S (hydrostatic with static initial sea-surface pulse), Nh-S (non-hydrostatic with static initial sea-surface pulse), and Nh-K (non-hydrostatic with kinematic seafloor excitation) approaches for unit slip of subfaults across the continental slop.

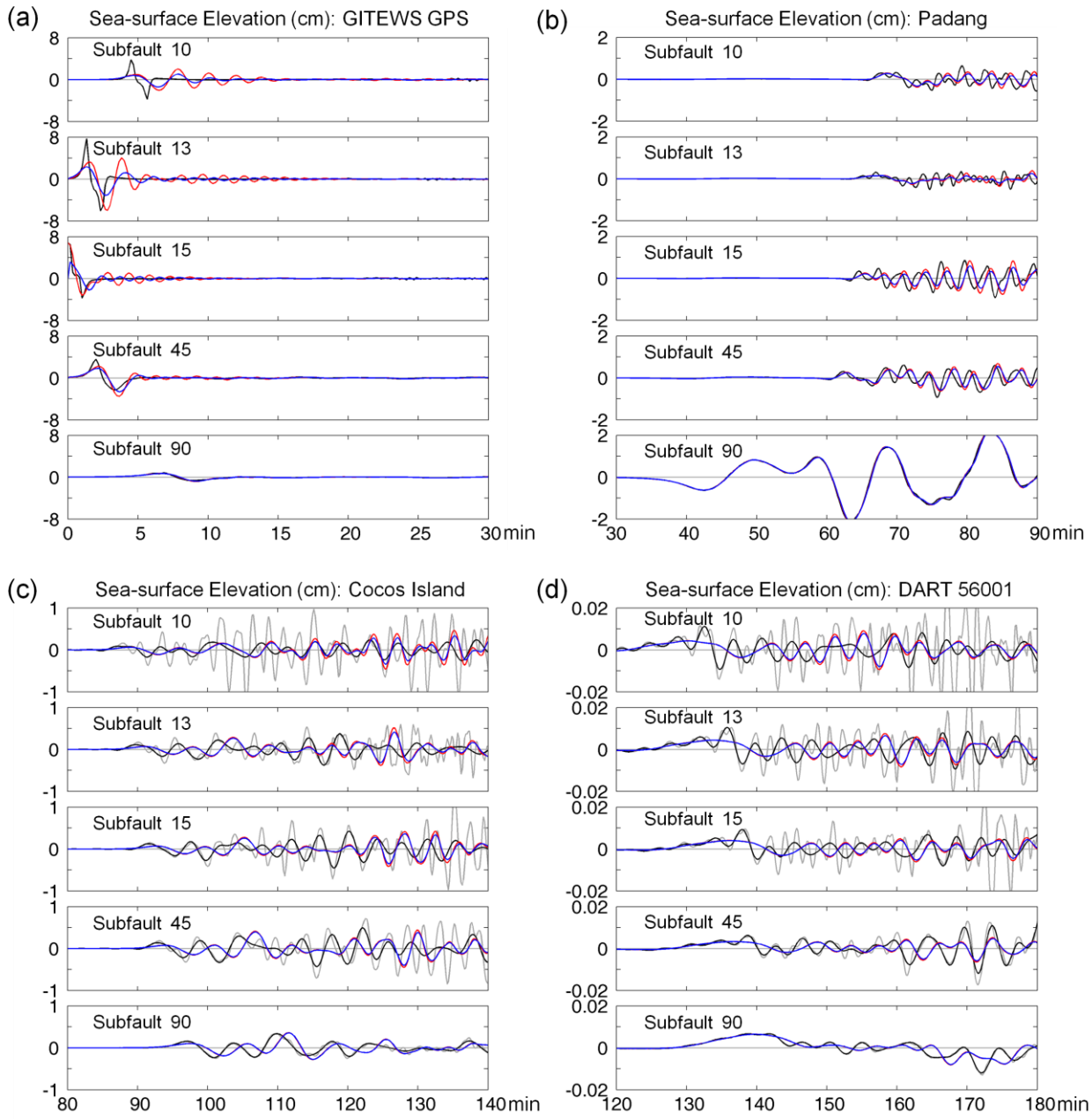

Figure 3. Green's functions at (a) GITEWS-GPS, (b) Padang, (c) Cocos Island, and (d) DART 56001 generated by the H-S (black), Nh-S (red), and Nh-K (blue) approaches. Kinematic seafloor excitation reduces the initial amplitude at the GITEWS GPS buoy in the near field, but has minor influences in the far-field. Due to limitations of a hydrostatic model in resolving short-period waves, high-frequency numerical oscillations accumulate during propagation. The H-S results at the far-field Cocos Island and DART stations are filtered to remove signals with periods less than 3 min (with the original data shown in grey).

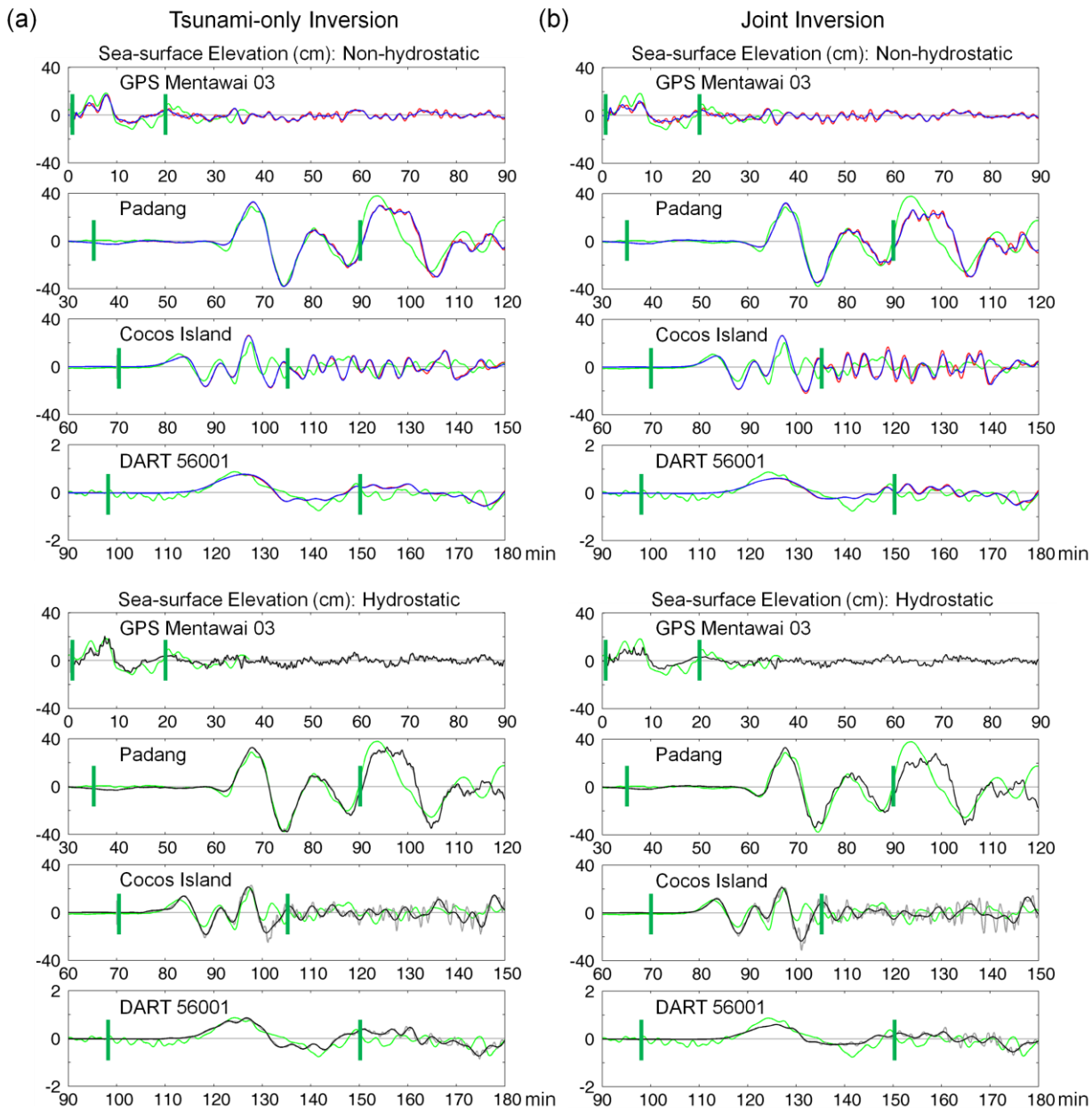

Figure 4. Tsunami waveform comparison for (a) tsunami-only and (b) joint inversions. Green lines denote recorded data, red and blue lines indicate computed waveforms from the Nh-S and Nh-K approaches, and black and grey are the H-S Green's functions with and without filtering. The vertical bars identify time windows of tsunami records used in the inversions.

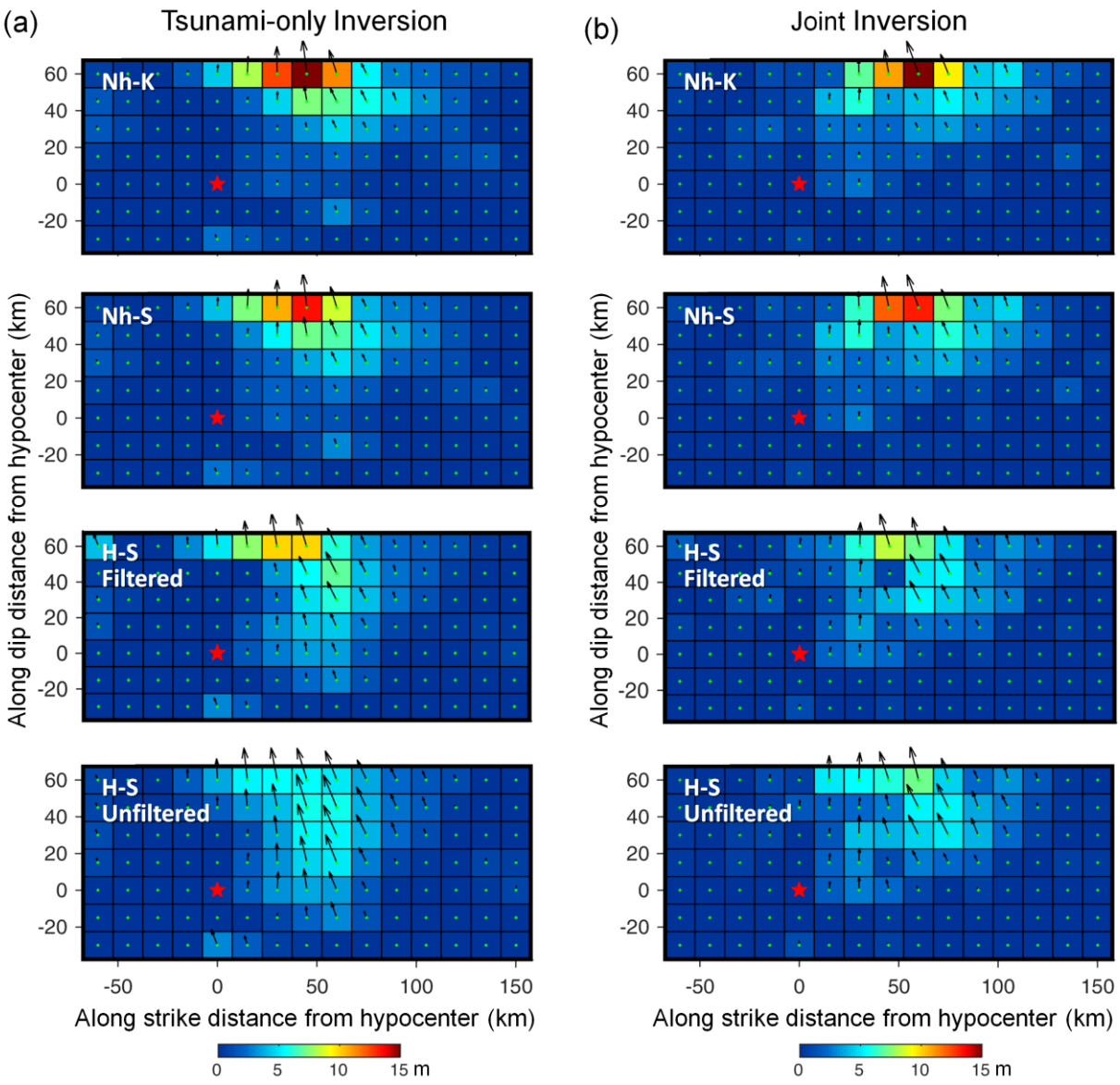

Figure 5. Slip distributions on the fault model grid inverted using tsunami Green's functions generated by the Nh-K, Nh-S, and H-S (filtered and unfiltered) approaches. (a) Tsunami-only inversion. (b) Joint inversion. Green's functions from non-hydrostatic modeling are necessary to resolve the large, concentrated near-trench slip consistent with the geodetic and seismic datasets.